Appendix A. Supplementary Figures

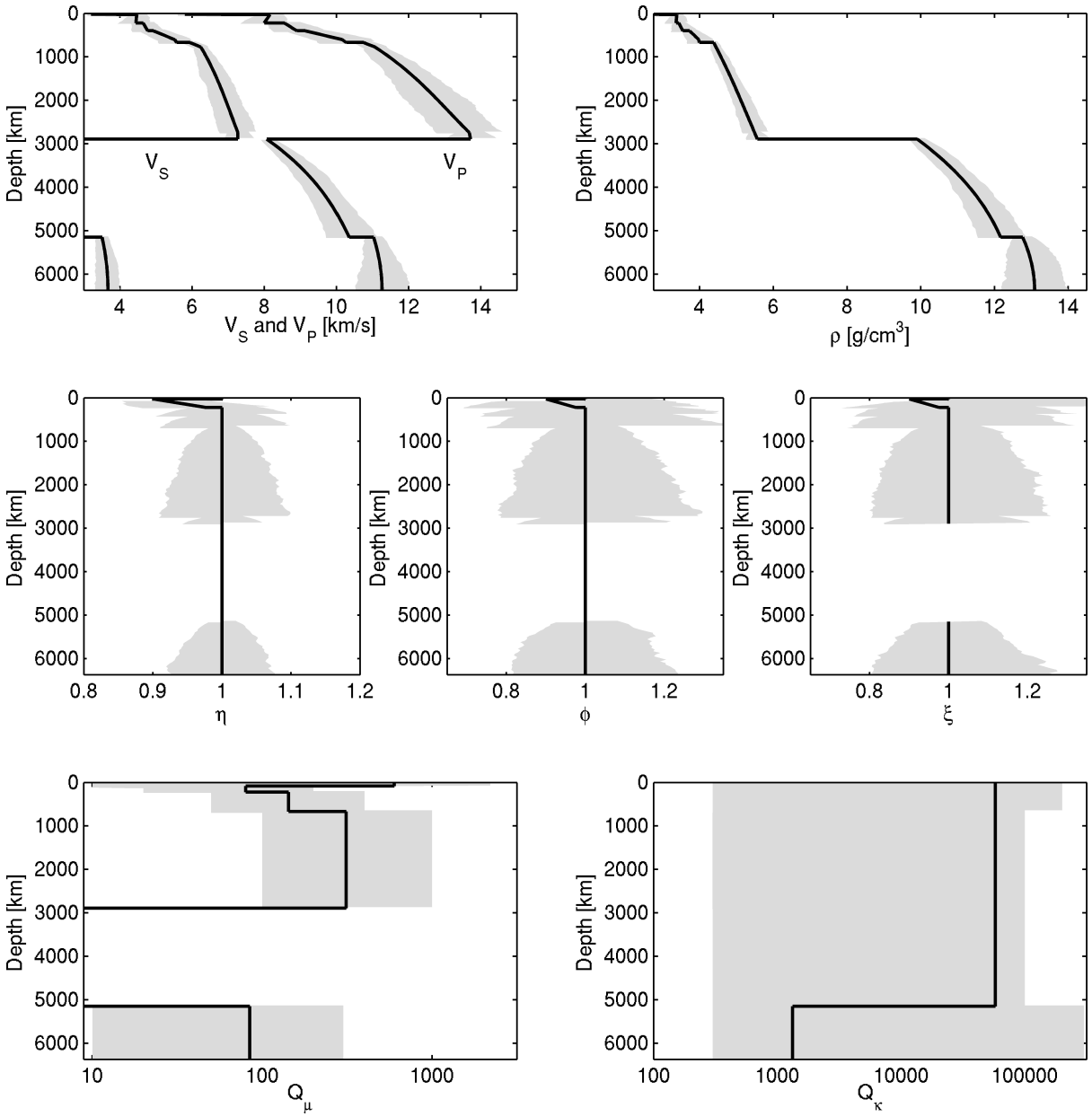

Figure A.1: Radial earth models contained in the model prior (see Section 2 and de Wit et al. (2014)). The parameter range spanned by the prior model space is represented by the grey shaded area, along with the 1-D reference model *PREM* (black, solid) for the Voigt average isotropic V_S and V_P (top-left panel), ρ (top-right panel), η (middle-left panel), ϕ (centre panel), ξ (middle-right panel), Q_μ (bottom-left panel) and Q_κ (bottom-right panel). The horizontal scale for the panels showing Q_μ and Q_κ is logarithmic. Note that the outer core is isotropic.

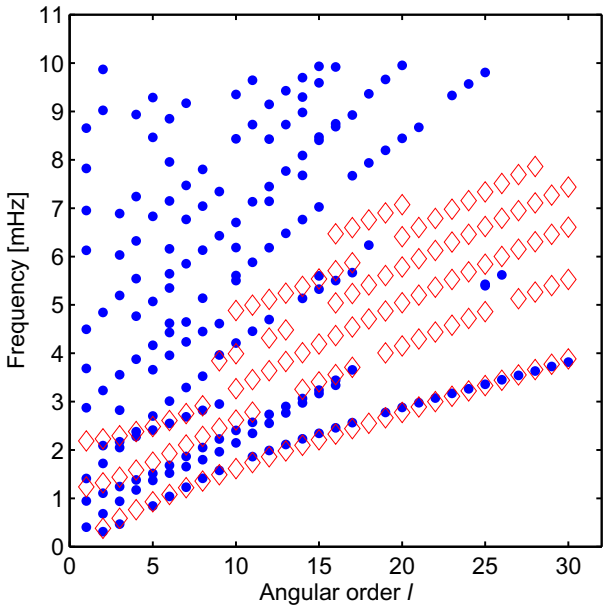

Figure A.2: Measured centre frequencies for the 184 spheroidal (blue dots) and 125 toroidal (red diamonds) modes (Section 4), as reported by Deuss et al. (2013); Koelemeijer et al. (2013); Koelemeijer (2014) and on the Reference Earth Model (REM) web pages (`http://igppweb.ucsd.edu/~gabi/rem.dir/surface/tmodes.list`), which form the input to the neural networks. Reported measurement uncertainties are on the order of μHz and therefore not shown.

Table A.1: Information gain D_{KL} in bits (Section 3.1) for target parameters representing averages in the five lower mantle layers and in the D" region. Note that the depths of discontinuities and the layer boundaries were allowed to vary between earth models (see Section 2 and de Wit et al. (2014)).

Layer	Depth [km]	$\bar{V}_P$	$\bar{V}_S$	$\bar{\rho}$	$\bar{\eta}$	$\bar{\phi}$	$\bar{\xi}$
LM_I	670–1027	6.8	4.6	5.8	1.4	9.3	9.2
LM_{II}	1027–1456	8.9	7.3	8.5	5.5	11.2	11.2
LM_{III}	1456–1884	9.5	7.9	9.6	8.7	10.8	12.1
LM_{IV}	1884–2313	9.7	10.1	10.1	9.8	10.9	11.8
LM_V	2313–2741	8.2	9.1	8.7	7.1	10.3	10.1
D"	2741–2891	2.8	2.4	0.3	0.1	1.9	2.6

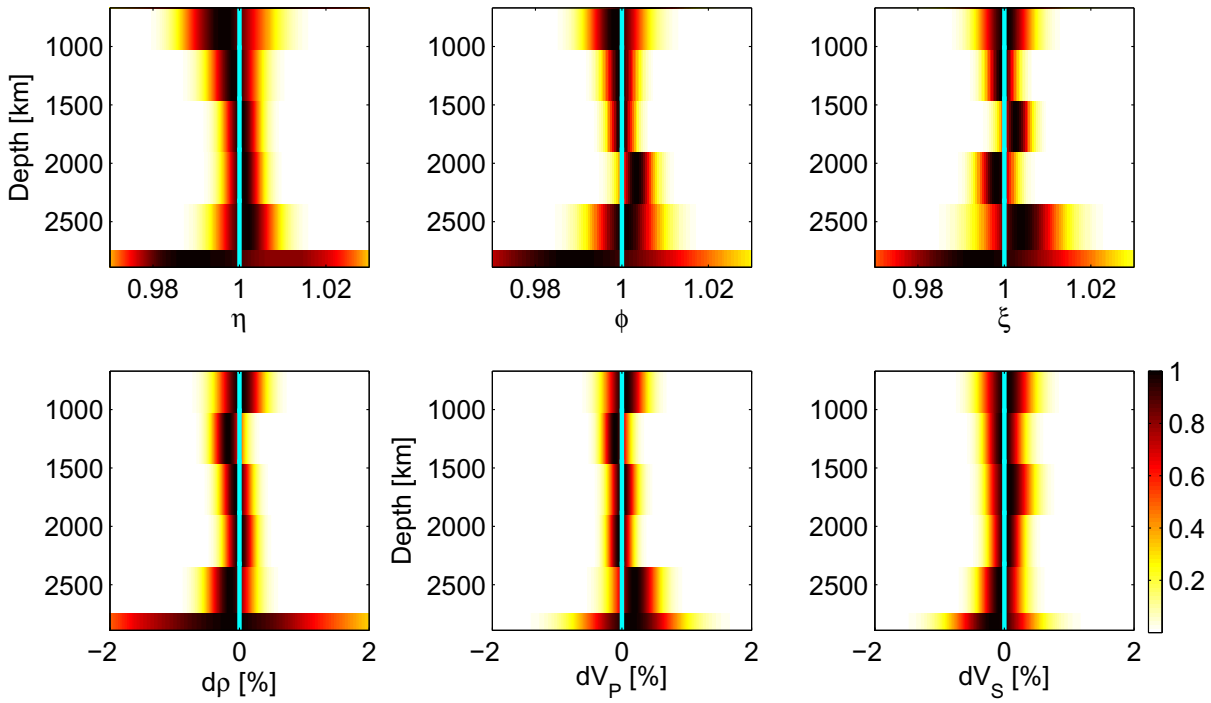

Figure A.3: 1-D marginal posterior pdfs for the inversion of synthetic *PREM* data for the averages of the six seismic parameters in the six lower mantle layers (Section 2). The bottom layer in each panel represents the D" region. *PREM* (cyan line) is isotropic in the lower mantle and is given as a reference. The velocities and density are expressed as percentage deviations with respect to *PREM*. The probability for each 1-D pdf is rescaled so that the maximum equals 1. Asymmetric 1σ and 2σ error bars correspond to the $1/e^{1/2}$ (0.61) and $1/e^2$ (0.14) contours, respectively. For all parameters, *PREM* lies within 1σ of the most probable value (the peak of the pdf).

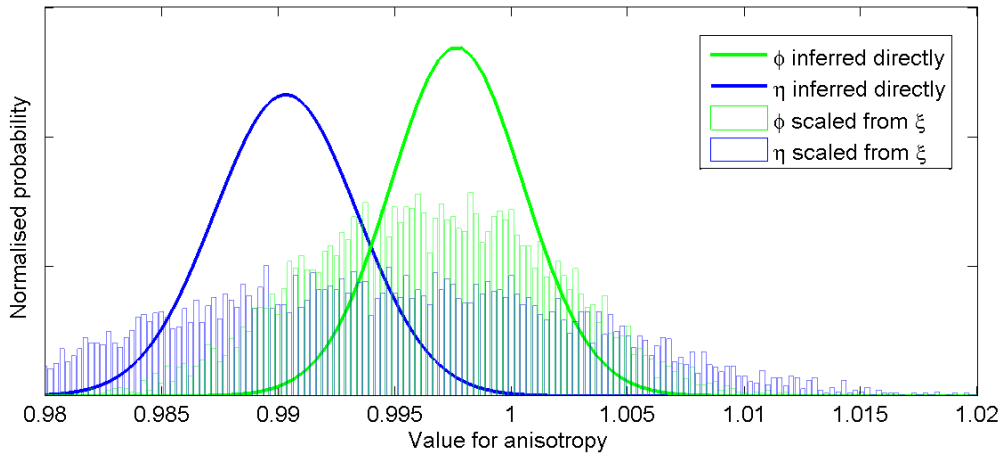

Figure A.4: Scaled 1-D marginals for ϕ (green histogram) and η (blue histogram) were constructed for lower mantle layer LM_{IV} (1884–2313 km) by resampling the corresponding 1-D marginal for ξ (Figure 1) and using scaling factors commonly assumed in the literature, i.e. $d\ln\phi/d\ln\xi = -1.5$ and $d\ln\eta/d\ln\xi = -2.5$ (Montagner & Anderson, 1989; Panning & Romanowicz, 2006). As a reference, we have added the 1-D marginals inferred from our inversion for this layer for ϕ (green line) and η (blue line), as shown in Figure 1.

Appendix B. Construction of polycrystal aggregates

We constructed a total of 22 491 thermochemical models using a polycrystal aggregate that is to first order representative of the lower mantle. The composition of the lower mantle in pyrolitic models usually constitutes ∼75% orthorhombic Mg-perovskite ($MgSiO_3$), ∼10% cubic Ca-perovskite ($CaSiO_3$) and ∼15% ferropericlase ((Mg,Fe)O) (Ono & Oganov, 2005; Mainprice, 2007). Alternatively, the nearly isotropic Ca-perovskite (Li et al., 2006) is often ignored, leading to a model with ∼80% Mg-perovskite and 20% ferropericlase. Laboratory and first-principles modelling studies show that both minerals are anisotropic under lower mantle conditions (Karki et al., 1997, 2000; Oganov et al., 2001; Wentzcovitch et al., 2004). Furthermore, a substantial amount of iron appears to be present in the lower mantle, partitioning into perovskite and ferropericlase, and is assumed to have a significant influence on the elasticity and other physical properties of these minerals (Mao et al., 1979; Kobayashi et al., 2005; Sinmyo & Hirose, 2013), An additional complexity arises when aluminium-bearing perovskite is added to the equation (Irifune, 1994; Nishiyama et al., 2007). We restricted our analysis to a polycrystal aggregate of aluminium-free and iron-bearing perovskite and ferropericlase and provided a first-order explanation of our seismic observations.

For each of the thermochemical models, we constructed the polycrystal aggregate in the following way. First, we varied the volume fraction of perovskite X_{Pv}, the volume fraction of iron X_{Fe} and the iron partitioning coefficient K_D (Table B.2). K_D controls the partitioning of the available iron into perovskite (Pv) and ferropericlase (Fp) and is defined as (Deschamps & Trampert, 2003; Kobayashi et al., 2005)

$$K_D = \frac{x_{Fe}^{Pv}/(1-x_{Fe}^{Pv})}{x_{Fe}^{Fp}/(1-x_{Fe}^{Fp})}, \tag{B.1}$$

where x_{Fe}^{Pv} and x_{Fe}^{Fp} are the volume fractions of iron in perovskite and ferropericlase, respectively. The total iron content is given by

$$X_{Fe} = X_{Pv} x_{Fe}^{Pv} + (1 - X_{pv}) x_{Fe}^{Fp}. \tag{B.2}$$

Using these two equations and the values given for X_{Pv}, X_{Fe} and K_D, we calculated x_{Fe}^{Pv} and x_{Fe}^{Fp} for each thermochemical model. We can fit the seismic observations for all three values considered for the partitioning factor K_D (Table B.2); we only show results for $K_D = 0.3$, which is a value typically assumed in the literature for aluminium-free systems (Deschamps & Trampert, 2004; Kobayashi et al., 2005; Lin et al., 2013).

Elasticity and density at lower mantle pressures were determined for pure-Mg orthorhombic perovskite (Wentzcovitch et al., 2004) and for cubic periclase (Karki et al., 2000). Wenk et al. (2006) used these estimates and associated temperature and pressure derivatives to obtain the elasticity at specified depths in the lower mantle. To first order, the elasticity and density change linearly with depth. Therefore, we linearly interpolated between the values reported in Table 2 of Wenk et al. (2006) to obtain the approximate elasticity and density at depths corresponding to the centre of our five lower mantle layers. This gave us the properties for the pure-Mg minerals at the five desired depths (Table B.3).

To correct the elasticity and density for iron, we used pure-Fe estimates for the two minerals (Jacobsen et al., 2002; Kiefer et al., 2002). Again, to first order the elasticity and density vary linearly between the Mg and Fe endmembers. Therefore, it is straightforward to calculate the properties of a (Mg,Fe)-mixture for perovskite and ferropericlase using the relation

$$a^{Pv,Fp}_{(Mg,Fe)} = a^{Pv,Fp}_{Mg}(1 - x^{Pv,Fp}_{Fe}) + a^{Pv,Fp}_{Fe} x^{Pv,Fp}_{Fe}, \tag{B.3}$$

where is $a^{Pv,Fp}$ is an element of the elasticity tensor or the density for Pv or Fp and $x^{Pv,Fp}_{Fe}$ is the volume fraction of iron for each of the two minerals, as calculated for each thermochemical model using Equations B.1 and B.2.

Second, we varied the temperature, in terms of a deviation from the Brown-Shankland geotherm (Brown & Shankland, 1981). We updated the elastic properties using the temperature derivatives $\partial a^{Pv,Fp}/\partial T$ estimated for perovskite (Wentzcovitch et al., 2004) and periclase (Karki et al., 2000) by applying the correction

$$a^{Pv,Fp} = a^{Pv,Fp} + T_{diff} \frac{\partial a^{Pv,Fp}}{\partial T}, \tag{B.4}$$

where $a^{Pv,Fp}$ is again an elastic property and T_{diff} is the temperature difference between our desired temperature, which is represented by a deviation ΔT from the Brown-Shankland geotherm (Table B.2) and the temperature used by Wenk et al. (2006) (their Table 2). The temperature along the Brown-Shankland geotherm, which corresponds to $\Delta T = 0$ k, is given for the centre of our five layers in Table B.3.

Third, we rotated the individual perovskite and ferropericlase crystals about the principal axes of their elastic tensors, which were aligned with the Cartesian reference frame (Walker & Wookey, 2012). We considered rotations about the two horizontal axes (x_1 and x_2) in 10 degree angles from 0 (no rotation) to 90 degrees. For each mineral, this gave 10^2 options; since we allowed the crystals to rotate separately, the total number of configurations became 10^4. Further, since rotations are not commutative, i.e. the order of rotation matters, we considered rotating in both orders $x_1 - x_2$ and $x_2 - x_1$, which gave a final number of $2 \cdot 10^4$ configurations for the rotation for each of the 22 491 thermochemical models.

Fourth, we calculated the Voigt average of the rotated elasticity tensors for the two minerals. The

Table B.2: Variation of compositional model parameters and temperature. The temperature is represented by a deviation ΔT from the geotherm by Brown & Shankland (1981), which is given for the centre of the five lower mantle layers in Table B.3. All possible combinations of these four parameters were considered, resulting in a total of 22 491 different thermochemical models.

Parameter	Minimum	Interval size	Maximum	No. of options
X_{Pv} [%]	50	1	100	51
X_{Fe} [%]	5	1	25	21
K_D	0.3	0.1	0.5	3
ΔT [K]	-200	50	100	7

Table B.3: Elastic constants and density for pure-Mg perovskite and periclase. Listed depths correspond to the centre of our five lower mantle layers. The elasticity at these depths was approximated by linearly interpolating between the values reported in Table 2 of Wenk et al. (2006). Also shown is the temperature along the geotherm by Brown & Shankland (1981), which corresponds to $\Delta T = 0$ K (Table B.2).

$MgSiO_3$-perovskite					
Depth [km]	849	1242	1670	2099	2527
Density [g/cm^3]	4.453	4.658	4.880	5.085	5.276
C_{11} [GPa]	578.2	642.6	706.3	774.9	851.5
C_{12} [GPa]	249.4	309.6	375.4	447.6	524.5
C_{13} [GPa]	228.9	274.4	323.8	372.9	426.6
C_{22} [GPa]	651.7	742.1	840.6	947.4	1062.7
C_{23} [GPa]	249.5	296.2	346.8	400.8	458.2
C_{33} [GPa]	619.8	720.3	823.6	931.4	1044.2
C_{44} [GPa]	202.7	225.7	249.7	273.2	298.6
C_{55} [GPa]	189.6	203.2	217.1	233.4	250.2
C_{66} [GPa]	175.4	202.0	229.3	256.3	284.1
MgO (periclase)					
Depth [km]	849	1242	1670	2099	2527
Density [g/cm^3]	3.981	4.219	4.457	4.668	4.870
C_{11} [GPa]	496.0	635.2	787.5	945.2	1108.5
C_{12} [GPa]	144.6	169.1	195.8	222.7	249.7
C_{44} [GPa]	159.0	169.8	179.4	188.1	196.3
Temperature [K]	1934	2055	2174	2279	2375

Voigt average assumes constant strain in the medium and places an upper bound on the true value of the elasticity (Voigt, 1910; Babuska & Cara, 1991; Mainprice, 2007). To facilitate a comparison with our seismic observations of radial anisotropy, we averaged the tensor for the polycrystal about the vertical axis (x_3) to impose vertical transverse isotropy (VTI), or radial anisotropy, using the approach by Walker et al. (2011); Walker & Wookey (2012).

Finally, we obtained a hexagonally symmetric elastic tensor for the polycrystal. It is trivial to extract η, ϕ, ξ and the Voigt average equivalent isotropic velocities V_P and V_S, as defined above, from the elastic tensor using the five independent Love coefficients A, C, N, L and F and the density ρ (Panning & Romanowicz, 2006; Mainprice, 2007). This enabled us to compare the values for the anisotropic parameters, density and wave velocities for each polycrystal aggregate with the 1-D marginal posterior pdfs that we obtained by solving the seismological inverse problem (Figure 1).

Note that for both orders of rotations about x_1 and x_2, we considered rotations about the vertical axis x_3 last; since we subsequently averaged about x_3, we did not need to investigate rotations about this axis. If x_3 would be one of the first two rotation axes, the elasticity tensor would be different. However,

the total number of permutations for a 3-D rotation vector is six, and more importantly, the number of configurations per mineral would be 10^3, resulting in a total of $6 \cdot (10^3)^2$ options for each thermochemical model. This was computationally infeasible and we limited ourselves to rotations about two of the three axes. For each of the 22 491 thermochemical models considered, this gave 10^4 configurations for each order of rotation, as noted above. Figure B.5 shows constraints on the rotation angles of the orthorhombic perovskite and cubic ferropericlase crystals for all the accepted thermochemical models and an order of rotation $x_1 - x_2(-x_3)$. For this order of rotation, no models were accepted in the second, third and fourth lower mantle layer (cf. Figure 3). For ease of comparison, we also visualised the accepted orientations using the more conventional Bunge Euler angles (Bunge, 1982), which can be easily derived from any rotation matrix. Since we only varied the rotation angle about the two horizontal axes (x_1 and x_2), we naturally did not consider all combinations of the three Euler angles. Figures B.6 and B.7 show constraints on the rotation, as represented by triplets of Bunge Euler angles, for both minerals and an order of rotation $x_2 - x_1(-x_3)$, corresponding to the constraints shown in Figure 3.

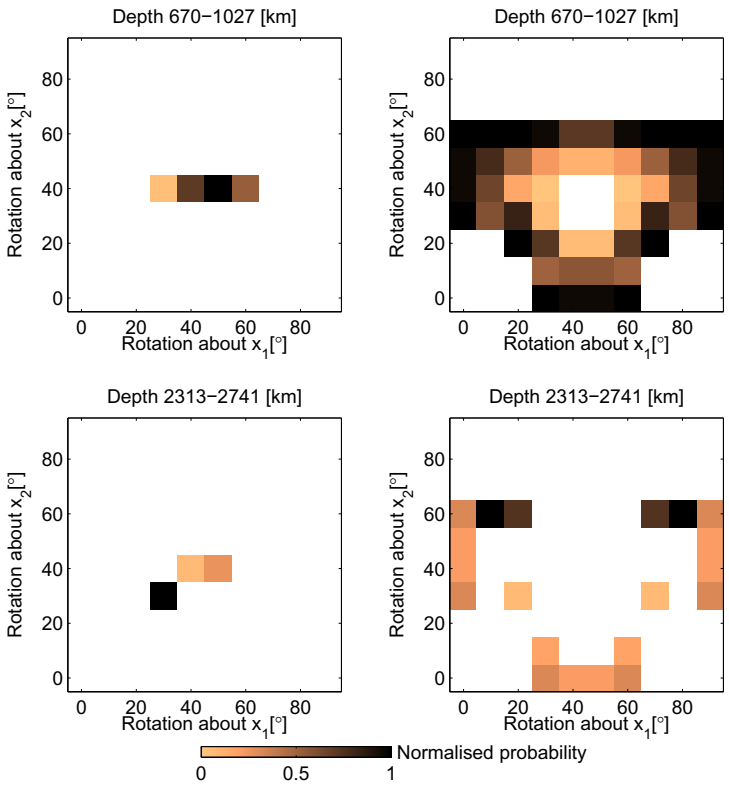

Figure B.5: Constraints on the orientation of the perovskite and ferropericlase crystals, represented by 2-D histograms of rotation angles for all accepted thermochemical models in the five lower mantle layers in D'. In each panel, the rotation angle about two principal (horizontal) axes x_1 and x_2 is shown for the orthorhombic perovskite (left) and cubic ferropericlase (right). The order of rotation was $x_1 - x_2(-x_3)$, where x_3 represents the vertical axis, over which we averaged to impose radial anisotropy. No models were accepted for the second, third and fourth layer for this order of rotation (cf. Figure 3). Each of the ten 2-D histograms is normalised, so that the colour indicates the relative number of accepted rotations. Empty cells represent rotation angles for which no thermochemical model fits all six seismic parameters within their uncertainties.

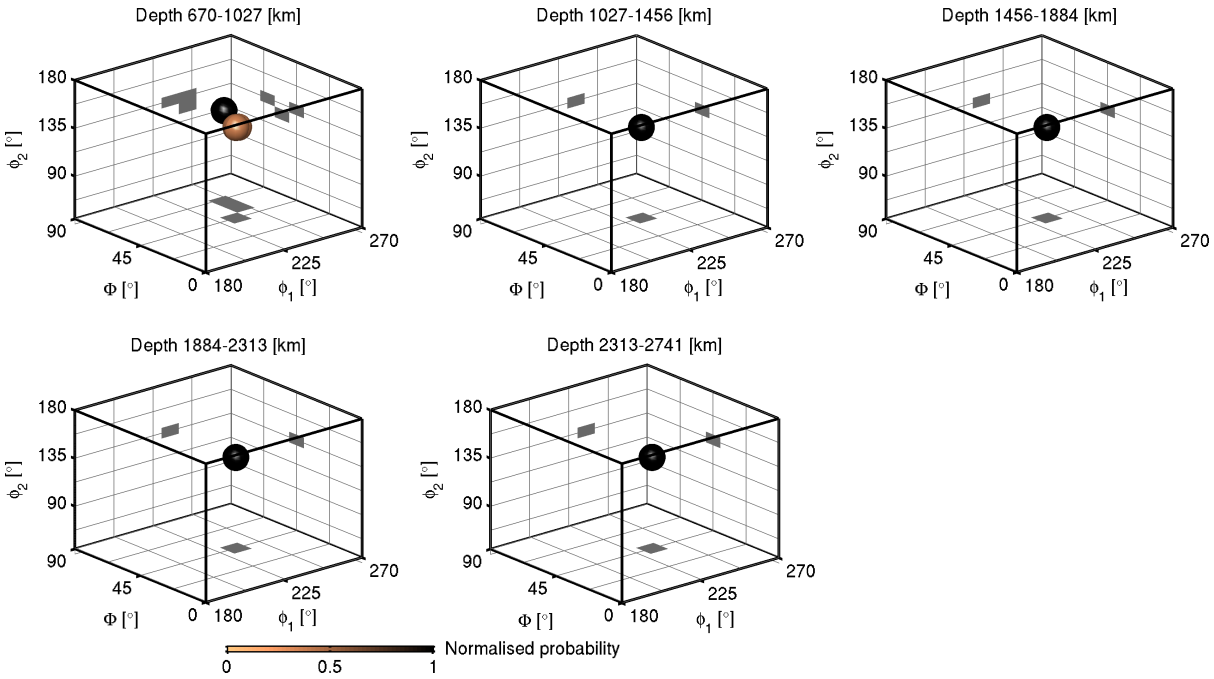

Figure B.6: Constraints on the orientation of perovskite crystals in the five lower mantle layers. Orientations are represented by Bunge Eugler angles (ϕ_1, Φ, ϕ_2, (Bunge, 1982)). The rotation angles for all accepted thermochemical models are shown as coloured spheres (voxels) and projected in grey, with the colour indicating the relative number of accepted rotations for each layer. Note that we performed the rotations about the two horizontal principal axes x_1 and x_2, and subsequently averaged over the vertical axis (x_3) to impose radial anisotropy (Figure 3). The more conventional Bunge Euler angles are only used for visualisation. The five boxes represent the five lower mantle layers, with the depth range given above each box.

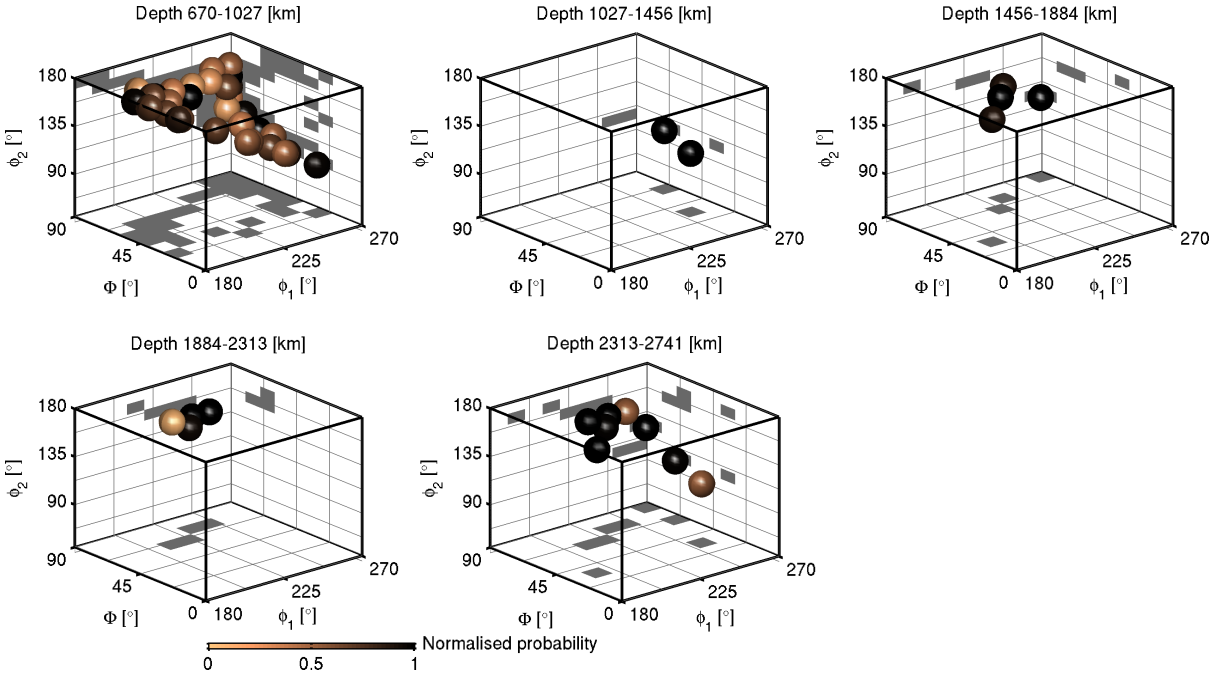

Figure B.7: Constraints on the orientation of ferropericlase crystals. See Figure B.6 for a description.